

Elemental Compositions of Comet 81P/Wild 2 Samples Collected by Stardust

G. J. Flynn¹, P. Bleuet², J. Borg³, J. Bradley⁴, F. Brenker⁵, S. Brennan⁶, J. Bridges⁴, D. E. Brownlee⁷, E. Bullock⁸, B. C. Clark⁹, Z.R. Dai⁴, C. Daghlain¹⁰, Z. Djouadi³, Sirine Fakra²³, T. Ferroir¹³, C. Floss¹¹, I. A. Franchi¹², Z. Gainsforth¹⁴, J.-P. Gallien^{WHERE?}, Ph. Gillet¹³, P. G. Grant⁴, G. A. Graham⁴, Simon F. Green¹², F. Grossemy³, P. Heck¹⁵, G. F. Herzog¹⁶, P. Hoppe¹⁵, F. Hörz¹⁷, J. Huth¹⁵, K. I. Ignatyev⁶, H. A. Ishii⁴, D. Joswiak⁷, A. T. Kearsley¹⁸, H. Khodja¹⁹, A. Lanzirotti²⁰, J. Leitner²¹, L. Lemelle¹³, H. Leroux²², K. Luening⁶, G. MacPherson⁸, K. K. Marhas¹¹, M. A. Marcus²³, G. Matrajt⁷, T. Nakamura²⁴, T. Nakano²⁵, M. Newville²⁰, D. A. Papanastassiou²⁶, P. Pianetta⁶, W. Rao²⁷, F. J. M. Rietmeijer²⁸, D. Rost⁸, C. S. Schwandt²⁹, T. H. See²⁹, J. Sheffield-Parker³⁰, A. Simionovici¹³, I. Sitnitsky¹, C. J. Snead¹⁴, F. J. Stadermann¹¹, T. Stephan²¹, R. M. Stroud³⁰, J. Susini², Y. Suzuki³¹, S. R. Sutton²⁰, S. Taylor³², N. Teslich⁴, D. Troadec²², P. Tsou²⁶, A. Tsuchiyama³³, K. Uesugi³¹, A. Westphal¹⁴, P. Wozniakiewicz¹⁸, E. Vicenzi⁸, L. Vincze³⁴, M. E. Zolensky¹⁷.

¹SUNY, Plattsburgh NY 12901 (george.flynn@plattsburgh.edu), ²ESRF, Grenoble, France,

³Institut d'Astrophysique Spatiale, Orsay, France, ⁴IGPP, Lawrence Livermore National Laboratory, Livermore CA, ⁵JWG-Univ. Frankfurt, Germany, ⁶Stanford Linear Accelerator Center, Menlo Park CA, ⁷Univ. Washington, Seattle, WA, ⁸Smithsonian Institution, Washington D.C, ⁹Lockheed-Martin, PO Box 179, Denver, CO 80201, ¹⁰Dartmouth College, Hanover NH, ¹¹Washington Univ, St. Louis, MO, ¹²Open Univ. Milton Keynes, UK, ¹³École Normale Supérieure de Lyon, Lyon, France, ¹⁴Univ. of California, Berkeley CA, ¹⁵MPI for Chemistry, Mainz, Germany, ¹⁶Rutgers Univ, Piscataway NJ, ³²NASA JSC, Houston, TX, ¹⁸NHM, London, UK, ¹⁹Lab. Pierre Süe, CEA/CNRS, Saclay, France, ²⁰Univ. Chicago, Chicago IL, ²¹Institut für Planetologie, Universität Münster, Germany, ²²Univ. Lille, Lille, France, ²³Advanced Light Source, Berkeley, CA, ²⁴Kyushu Univ, Fukuoka, Japan, ²⁵AIST/GSJ, Ibaragi, Japan, ²⁶Jet Propulsion Laboratory, Pasadena, CA, ²⁷Univ. Georgia, Athens, GA, ²⁸Dept Earth & Planetary Sciences, Univ. of New Mexico, Albuquerque, NM 87131, ²⁹ESCG/NASA JSC, Houston, TX, ³⁰U.S. Naval Research Laboratory, Washington, DC 20375, ³⁰XRT Ltd, Port Melbourne, Australia, ³¹JASRI/SPring8, Hyogo, Japan, ³²ERDC-CRREL, Hanover, NH, ³³Osaka Univ, Japan, ³⁴Ghent Univ, Ghent, Belgium.

ABSTRACT: We measured the chemical compositions of material from 23 particles in aerogel and residue in 7 craters in aluminum foil, collected during passage of the Stardust spacecraft through the coma of Comet 81P/Wild 2. These particles are chemically heterogeneous at the largest size-scale analyzed, ~180 nanograms. The mean chemical composition of this Wild 2 material agrees with the CI meteorite composition for the refractory elements Mg, Si, Cr, Fe, and Ni to 35%, and for Ca and Mn to 50%. The data suggest the moderately volatile elements Cu, Zn, and Ga may be enriched in this Wild 2 material.

NASA's Stardust spacecraft collected dust particles from Comet 81P/Wild 2, at an encounter speed of ~6.1 km/s, into low-density, silica aerogel capture cells and in impact craters in the Al-

foils that covered the supports of the aerogel holder (1). A primary objective of the Stardust mission is to determine the chemical composition of the Wild 2 particles, and to compare it with those of other extraterrestrial materials.

Methods: High speed particle impacts in aerogel produce elongated cavities called tracks. Keystones, triangular wedges of aerogel containing an entire track (2), were extracted from the Stardust capture cells. The volume containing each track was analyzed using Synchrotron-based X-Ray Microprobes (SXRMs), providing X-ray fluorescence chemical analysis for elements having atomic number ≥ 16 ($Z \geq 16$). One track was subsequently split open, exposing the wall for analysis by Time-of-Flight Secondary Ion Mass Spectrometry (ToF-SIMS), a surface analysis technique allowing detection of lower-Z elements, particularly Mg and Al. Since Si and O are the major elements in silica aerogel, neither element could be determined in the tracks. Major elements in the residues in craters were determined using Energy Dispersive X-ray analyses (SEM-EDX) and ToF-SIMS. The crater residues provide information on light elements, including Mg and Si, that could not be determined in the SXRMs analysis of tracks, but the contribution of Al from the comet could not be determined because of the Al signal from the foil. Combining analytical results from the cometary material in the tracks and in the craters provides a more comprehensive chemical analysis of the Wild 2 particles.

Tracks in Aerogel: Keystones containing 23 particle tracks, selected to sample the diversity observed visually on the Stardust collector, were analyzed using SXRMs (3). These tracks ranged in length from ~250 to almost 10,000 μm , and varied in shape from almost perfect conical tracks to bulb-like tracks. In many cases, several fragments emerge from the bulb producing their own conical tracks. Particles collected during passage through the dust coma of Wild 2 impacted normal to the front surface of the aerogel (1), while interplanetary dust particles, which may also have been collected, arrived over a wide range of orientations. All 23 tracks were approximately normal to the aerogel surface.

Element analysis of 23 tracks in keystones was performed by six groups using five different synchrotrons. Tracks were analyzed by two different and complementary methods. Some keystones were analyzed by mapping the entire track and surrounding area, collecting an entire fluorescence spectrum at each point on a raster scan, using a long integration times. Other keystones were analyzed by rapidly scanning a track, identifying “hot-spots” in Fe fluorescence, then integrating for long times on these hot spots. The first technique is more comprehensive, while the second technique is more sensitive for trace elements. Mean compositions obtained using the two techniques are generally very similar (see supplementary material for a detailed discussion.)

An example of the analysis of one track is shown in Figure 1. Maps of the K-alpha fluorescence intensity for Fe, Ni, Zn, and Cr from Track 19, a cone-shaped track ~860 μm long from aerogel cell C2115. The track is well-defined in the Fe map, indicating that the incident particle deposited Fe along much of the entry path as it decelerated in the aerogel. Most of the Fe in the Track 19 map is detected along the track wall, with only 3% of the total Fe being concentrated in the terminal particle.

The fraction of the total Fe detected in the terminal particle varies from track to track, with two tracks having no detectable terminal particle in any of the element maps, while one track has almost 60% of its Fe mass in the terminal particle. In most of the 23 tracks examined, the majority of the incident Fe mass is deposited along the entry track, indicating that the particles are generally relatively friable, more comparable in their aerogel capture behavior to that seen in test shots of very weak meteorites, like Orgueil, rather than stronger meteorites like Allende.

The spatial distributions of individual elements in each track vary widely. Nickel is deposited along the entire length of Track 19. The Ni/Fe ratio summed over the whole track is 0.041,

within 50% of the CI ratio of 0.058 (4). However, Ni/Fe is much lower (Ni/Fe = 0.0062) in the terminal particle. Zinc is concentrated along one edge of the track, with almost none detectable in the terminal particle, but almost 80% of the total Cr is in the terminal particle. Considerable element heterogeneity is seen in most of the 23 tracks examined, indicating that many of the Wild 2 particles were aggregates of material having diverse compositions.

The aerogel contains trace quantities of virtually all stable elements (1), and several are found in hot-spots (5). This contamination results in higher detection limits, and the heterogeneity makes background subtraction difficult. The widespread distribution of compositionally diverse comet material along each track required that we develop a variety of analytical strategies to yield the most comprehensive element data possible. The simple technique of extracting the terminal particle for analysis with a electron microprobe provides little information on the bulk composition of the comet.

The terminal particle and the 19 most intense element hot-spots along Track 19 were analyzed individually. Increased sensitivity obtained by using much longer analysis times for each spot than the dwell time per pixel in the mapping. The element/Fe ratio in each spot analysis was normalized to the CI chondritic meteorite composition (4), which is thought to represent the mean non-volatile composition of the Solar System (6). The CI and Fe normalized element abundances for these 20 spots are shown in Figure 1. Most element/Fe ratios vary by two orders-of-magnitude or more from spot to spot along the track.

A “whole track” composition was determined by adding the element abundances from the 19 analyses along the track to that of the terminal particle (5). The Fe-normalized whole track composition for Track 19 (Figure 1) is consistent with CI for S, Cr, Mn, and Ni, but enriched in the moderately-volatile elements Cu, Zn, Ga and Se, and depleted in Ca and Ge.

No single mineral found in terrestrial or extraterrestrial material has a CI composition. Thus, observing a CI composition indicates that the particle is an aggregate of compositionally diverse grains that sum to a CI composition. This is consistent with the high variability in the 20 spot analyses of Track 19.

Anhydrous silicate minerals (typically olivine and pyroxene) in most primitive extraterrestrial materials contain very low abundances of Ni and moderately-volatile minor elements compared to CI. In the majority of the tracks analyzed, Ni/Fe is significantly lower in the terminal particle than in the whole track (as shown in Figure 1 for Track 19). The chemical compositions of many of the terminal particles are consistent with their domination by a single mineral -- olivine, Fe-sulfide, or Fe-metal, consistent with the proposition that individual mineral grains have a higher chance of survival as terminal particles than do aggregates.

To obtain information about low-Z elements not measurable in the SXRMs analyses, the bulb portion of one keystone, Track 21 from cell C2115, was dissected laterally to expose the track wall. Two slices were analyzed by ToF-SIMS. These analyses indicate that Mg/Fe, Al/Fe, Cr/Fe, and Mn/Fe are within 50% of CI (5).

Residue in Impact Craters: Impact residue, which is abundant in all large craters in the Al-foils examined thus far, provides chemical composition data complementary to that obtained on the tracks and allow direct measurement of major element to Si ratios. Although the Al-foil contains indigenous iron inclusions, occasional silicon-rich inclusions, and a wide range of trace elements (9), unambiguous impact residue of micrometer scale was easily located in craters by both SEM-EDX and ToF-SIMS.

To assess element loss during crater production, a variety of projectiles were fired, at ~6 km/sec, into the same Al1100 foil carried by the Stardust spacecraft. In craters >50 μm in diameter the loss of Na, Mg, Si, and Fe was small (5, 9), so analysis of residue in craters of this size is

expected to provide a good sample of the composition of the comet dust that impacted the spacecraft.

The chemical composition of the residue in seven large craters, each having a top-lip diameter $>50\ \mu\text{m}$, from the Stardust Al-foils have been characterized using SEM-EDX. In each case, the mass of the impacting particle was estimated using the crater size calibration of Kearsley et al. (10) with a suitable scaling for particle density, based upon the particle mineralogy inferred from the chemical composition measurement. The estimated masses of the impacting particles range from 3 nanograms to 178 nanograms, with 6 of the 7 craters having impactor masses of 17 nanograms or less. The residues in 5 of these craters were also analyzed by ToF-SIMS.

In addition to the large craters, an SEM survey of the Al-foils identified numerous smaller impact craters, generally less than $2\ \mu\text{m}$ in diameter. The original cometary projectiles would range from $\sim 400\ \text{nm}$ down to $20\ \text{nm}$ in diameter (10). SEM-EDX chemical analysis of several hundred craters identified compositional groups consistent with impacting particles composed of silicates, sulfides, and mixtures of silicate and sulfide (11). These small craters show an increased abundance of S, but the cumulative mass-frequency distribution of the impacting particles (11) indicates that most of the mass collected at Wild 2 is in larger projectiles and that the total mass of material in these small craters is inadequate to substantially alter the element abundance pattern.

Data Analysis: The total Fe detected along the 23 tracks ranges from about 180 femtograms to 6.4 nanograms, comparable to the Fe in an $1\ \mu\text{m}$ and a $30\ \mu\text{m}$ chondritic particle of $1\ \text{gm/cc}$ density respectively. Most of the CI normalized whole track element/Fe ratios, shown in Figure 2, exhibit variations of more than two orders-of-magnitude from track to track. Thus, a reliable mean composition can only be determined by averaging many particles.

In no case can we be certain that we analyzed all the material from any incident particle. Some material is certainly lost in crater formation. The extent to which vaporized material can be lost through the entry hole of a track has never been investigated. Vaporized material may also penetrate many track diameters through the aerogel, as observed for some organic matter in Stardust tracks (REF SANDFORD). In addition, the spot analysis employed for 9 of the tracks only analyzed material in these hot spots. Two tracks analyzed by both mapping and hot-spot techniques using the same SXRm show good agreement for most coincident elements: For Track 12 (NSLS) Mn/Fe, Ni/Fe and Cr/Fe $< 30\%$ difference (5); Track 19 (APS), Mn/Fe, Ni/Fe and Zn/Fe $< 25\%$, Cr/Fe and Cu/Fe \sim a factor of two. Differences may result from the hot-spot technique analyzing a smaller fraction of the total material than the mapping method. The Cr/Fe, Mn/Fe and Ni/Fe whole track results for Track 12 using two different x-ray microprobes show a similar level of agreement (5). We also looked for systematic differences between the two methods, and concluded that any systematic differences are smaller than the statistical errors in each set of data (5).

We determined the mean composition by summing the measured abundance of each element over all 23 tracks. Except for Fe, no element was detected in all tracks. Nickel was detected in 22 tracks, S in 21, Ca, Cr, Mn and Cu in 20, Zn in 17, Ga in 14, Ti and Se in 9. When an element was not detected, it was included in the sum as zero.

There are four major sources of error in the mean composition of the Wild 2 particles that produced the tracks and craters we analyzed:

- 1) the uncertainty resulting from averaging only a small number of events having extremely diverse compositions.
- 2) The absorption corrections for low-Z elements, particularly S, in the capture medium and the particles themselves,
- 3) the precision and accuracy of the analyses,

- 4) the extent to which the material we analyzed is representative of all the material in the initial particle.

Element abundances at each spot, generally determined by comparison of the fluorescence intensity to the fluorescence intensity of NIST standards analyzed under the same conditions, are accurate to $\pm 20\%$ for the elements having $Z \geq 24$ (Cr) (5). The largest uncertainty in the mean composition is likely to result from the high degree of compositional heterogeneity from particle to particle. To estimate the confidence limit on the mean composition we used a Monte Carlo method. We assumed that the observed distribution of particle sizes and compositions of the 23 measured tracks is characteristic of the entire dust population hitting the collector. We then generated a large ensemble (10,000) of data sets of 23 tracks by randomly drawing tracks, one at a time, from the observed data set. We then determined 1-sigma and 2-sigma confidence limits from the distributions of element ratios in these randomly-generated ensembles (5).

The CI- and Fe-normalized mean element abundances and the 1-sigma confidence limits are given in Table 1. The same data is plotted in Figure 3, but the 2-sigma confidence limits are shown. One of the tracks, Track 7 from C2044, contributed $\sim 30\%$ of the total Fe. However, its inclusion does not distort the average, since the average excluding Track 7 does not differ significantly from the 23 track average (see Figure 3).

Most element/Fe ratios are consistent with the CI ratios at the 1-sigma confidence level. The exceptions are S, which is apparently significantly depleted, and Cu, Zn, and Ga, which appear to be enriched. Each of these deviations is addressed in the Discussion section.

Although we analyzed residue in 7 craters, only Mg, Si, and Fe were detected in all of the craters. Chromium was detected in 4 of the craters, Na in 3, and P, K, Mn, and Ni in only 2. The CI and Si normalized mean composition for elements detected in 4 or more craters, determined by adding the compositions of the crater residues, is shown in Figure 4. Since the largest crater was produced by a particle having 82% of the total mass of the 7 particles, the average composition for the 6 smaller craters is also shown in Figure 4. We determined confidence limits on the mean abundances in the crater data by the same Monte Carlo technique that we used for the track data. Because of the small number of craters analyzed, the statistical uncertainty on the mean is large.

The mean CI- and Si-normalized element abundances and the 1-sigma confidence limits, given in Table 2, appear to deviate significantly significantly from the CI composition for all elements reported in Table 2 at the ~ 2 -sigma level (see Figure 4). The elements with less than 4 measurements, Mn (mean value $1.2 \times \text{CI}$), K ($0.7 \times \text{CI}$), Na ($1.6 \times \text{CI}$), and Ni ($0.2 \times \text{CI}$), were not reported in Table 2 because confidence limits were difficult to determine with so few detections. The apparent S depletion is consistent with the results from the tracks.

The CI- and Fe-normalized average element abundance derived from the ToF-SIMS analyses is also shown in Figure 4. This mass-weighted average composition is consistent with CI for Mg, Ca, and Mn, while there are small depletions, relative to CI, for Fe and Ti, and a larger depletion for Ni, consistent with the SEM-EDX results on the larger set of 7 craters. However, the ToF-SIMS results are an order-of-magnitude higher than the SEM-EDX results for Na and K, elements that may mobilize on impact. This difference may result from SEM-EDX measuring microns into the residue, predominately at the crater bottom, while ToF-SIMS measures only material sputtered from the surface mainly from the crater lip (5).

Discussion: The size at which the composition of an aggregate converges to the average composition is an indication of the grain-size of the material. Fine-grained, chondritic interplanetary dust particles (IDPs) (7) are aggregates of submicron grains, typically containing 10^4 to 10^5 grains in a $10 \mu\text{m}$ particle. These IDPs generally show only a factor of two variation in major elements and less than a factor of 5 variation in minor elements in $\sim 10 \mu\text{m}$ size particles (8).

Primitive chondritic meteorites, which have a much larger mean grain size, show a significantly greater variation in their chemical compositions in samples up to millimeters in size. The Wild 2 particles show greater compositional diversity than the $\sim 10\ \mu\text{m}$ fine-grained IDPs. Since both the largest track and the largest crater have compositions significantly different from the mean composition, the comet appears to be chemically heterogeneous at the largest size scale we analyzed.

Prior to the Stardust mission, the only direct measurement of the elemental composition of the dust from a comet came from impact-ionization mass-spectrometers (12) that flew through the dust coma of comet Halley on the Giotto and the two VEGA spacecraft in 1986. Although the impact ionization yields are uncertain, the results indicate that the mean abundances of the major rock-forming elements (**LIST THEM FROM JESSBERGER'S PAPER**) in the dust from comet Halley are within a factor of two of the CI meteorite abundances (13), a result based on the analysis of <1 nanogram of cometary material. Spectroscopy of cometary meteors indicates element abundances in Leonid and Perseid meteoroids consistent with CI for Na, Mg, Si, Ca, Cr, Mn and Fe (14).

The Wild 2 particles in the 23 keystones contain ~ 21 nanograms of Fe. Assuming a CI content of Fe (~ 18.2 wt-%), the total mass of Wild 2 material in these tracks is ~ 115 nanograms. The crater residue resulted from the impact of ~ 215 nanograms of material. Taken together, we analyzed material deposited in aerogel and craters by >300 nanograms of comet particles, a mass several orders-of-magnitude more than previously analyzed in-situ at comet Halley.

Our composition results for the Wild 2 particles are consistent with the Halley measurements, but greatly extend those measurements. The larger sample mass coupled with the ability to analyze this material using high-sensitivity instruments in state-of-the-art laboratories on Earth significantly extends the quality of the chemical analysis that can be performed. For example, the trace elements Cu, Zn, Ga, Ge and Se have been measured for the first time in dust from an identified comet.

Sulfur appears to be depleted ($S = 0.17 \times \text{CI}$) in both the track and crater analyses. The statistical significance of this depletion is very high (>3 -sigma). However, in the case of the track analyses, the low-energy S fluorescence x-rays are attenuated by a few microns of a high density mineral (e.g., Fe-sulfide) or compacted aerogel. Since most keystones are 200 to 300 μm thick, a first-order correction, made assuming all the S is shielded by 100 to 150 μm of 20 mg/cc aerogel (REF DESCRIBE ACTUAL STARDUST AEROGEL), would increase the S by no more than a factor of 2. But, some S is observed to be finely distributed in compacted or melted aerogel (REF MIN PET PAPER), so the full effect of attenuation cannot be assessed without a detailed knowledge of the shape/size of this aerogel along each track.

Selenium abundance is well-correlated with S in meteoritic minerals. Although we detected Se in only 9 tracks, the mean Se abundance is $1.02 \times \text{CI}$, taking the non-detections as zero. The Se/S ratio in the whole track that has the highest S abundance (Track 77) is 0.0023, 6.4 times the CI Se/S ratio (4). If S and Se are correlated in the Stardust particles and have similar behavior during capture, then S in the whole track data may have been underestimated. Attenuation of the Ca fluorescence is much less severe, and the other elements we report have minimal attenuation in material of this thickness.

Even increasing the S by a factor of 2, required to correct for the aerogel absorption in the track analyses, does not provide consistency with CI at the 2-sigma level. Among the 5 CI meteorites that contribute to the CI average (Lodders, REF), S varies by almost 30% on a much larger sample than the mass of Wild 2 material analyzed. In addition, **while the other major elements vary by less than a factor of two between the CI and ordinary chondrites, S varies by an order-of-magnitude (CHECK THIS)**. Since only 10% of the Stardust aerogel cells and a comparable (IS

IT?) fraction of the Stardust Al-foils have been examined, comprehensive chemical analyses of the remaining material that was collected, including the largest tracks, not yet studied, should provide a better understanding of the mean S content and decrease the uncertainty in other element abundances.

The Wild 2 material analyzed appears enriched in the moderately-volatile elements (Cu, Zn, and Ga) compared to CI, an effect that was previously reported in the fine-grained, anhydrous IDPs (REF FLYNN ET AL.), some of which have inferred atmospheric entry speeds suggesting a cometary origin (Brownlee et al., 1993). The CI meteorite element abundances are taken to represent the Solar Nebula composition for non-volatile elements because of the good agreement between CI abundances and the composition of the Solar photosphere, measured by spectroscopy (REF AANDERS AND GREVESSE). However, the abundances of Cu, Zn, and Ga are not well determined in the Solar photosphere (ref Anders and Grevese, 1989), suggesting the possibility that abundances of these elements in the Wild 2 particles and the anhydrous IDPs may better reflect the composition of the Solar Nebula for these moderately-volatile elements.

Stardust encounters comet 81P/Wild 2

Authors:

Tsou, P.; Brownlee, D. E.; Anderson, J. D.; Bhaskaran, S.; Chevront, A. R.; Clark, B. C.; Duxbury, T.; Economou, T.; Green, S. F.; Hanner, M. S.; Hörz, F.; Kissel, J.; McDonnell, J. A. M.; Newburn, R. L.; Ryan, R. E.; Sandford, S. A.; Sekanina, Z.; Tuzzolino, A. J.; Vellinga, J. M.; Zolensky, M. E.

Publication:

Journal of Geophysical Research, Volume 109, Issue E12, CiteID E12S01 (JGRE Homepage)

Publication Date:

12/2004

2. A. J. Westphal, C. Snead, A. Butterworth, G. A. Graham, J. P. Bradley, S. Bajt, P. G. Grant, G. Bench, S. Brennan, and P. Pianetta, *Meteoritics & Planetary Science*, 39, 1375-1386 (2004).

3. XRM review article

5) K. Lodders, *Ap.J.*, 591, 1220-1247. (2003)

6) See Supporting Materials Online

7) Anders and Grevese

8) Brownlee 1985 review of IDPs

9) 8) Flynn and Sutton COMPOSITIONAL VARIABILITY OF IDPS

10) Kearsley 2006b

11) Kearsley 2006a

12) Horx Crater Paper this issue of Science

- 13) Kissel (1986, Mass Spectrometric Studies of Halley Comet,” *Advances Mass Spectroscopy*, **1985**, 175-184)],
- 14) Jessberger et al., 1988
- 15) **[REFERENCE: Borovicka, J. (2004) Elemental abundances in Leonid and Perseid meteoroids. *Earth, Moon, and Planets* **95**, 245-253.]**

AEROGEL REF: To optimize the capture of particles spanning a large range of masses in aerogel that was restricted to a depth of 3 cm, graduated-density silica aerogel was fabricated for the Stardust mission. Near the exposed surface this aerogel has a very low density (5 to 10 mg/cc), increasing to 20 mg/cc, and then increasing again to 50 mg/cc towards the rear of the capture cell. The low density aerogel at the surface allows the smallest particles to decelerate slowly, while the high density aerogel at the rear allows the capture of particles >100 μm in diameter.

References: [1] Tsou, P. et al. (2003) *JGR*, **108**, E10, 3.1-3.21. [2] Westphal, A. et al. (2004) *Meteor. Planet. Sci.*, **39**, 1375-1386. [3] SXRf reference on track analysis.

Table 1: CI- and Fe-normalized mean composition of the 23 tracks in aerogel, with 1-sigma confidence limits.

S	$0.17^{+0.12}_{-0.06}$	Ca	$1.25^{+0.47}_{-0.43}$	Ti	$0.42^{+1.74}_{-0.23}$
Cr	$1.30^{+0.24}_{-0.31}$	Mn	$1.32^{+0.32}_{-0.37}$	Ni	$0.82^{+0.37}_{-0.24}$
Cu	$2.06^{+1.14}_{-0.69}$	Zn	$4.6^{+6.3}_{-3.1}$	Ga	$10.0^{+8.9}_{-7.5}$
Ge	$0.43^{+1.46}_{-0.22}$	Se	$0.76^{+1.51}_{-0.42}$		

Table 2: CI- and SI-normalized mean composition of 7 crater residues in Al-foil, with 1-sigma confidence limits.

Mg	$1.13^{+0.22}_{-0.05}$	S	$0.13^{+0.40}_{-0.06}$	Ca	$0.51^{+0.12}_{-0.05}$
Cr	$0.31^{+0.31}_{-0.04}$	Fe	$0.75^{+0.05}_{-0.40}$		

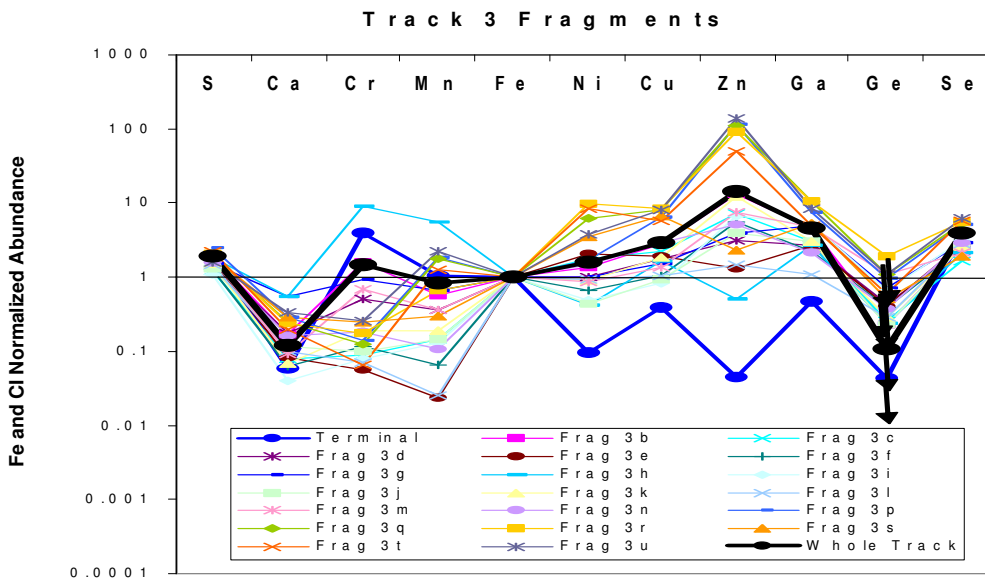
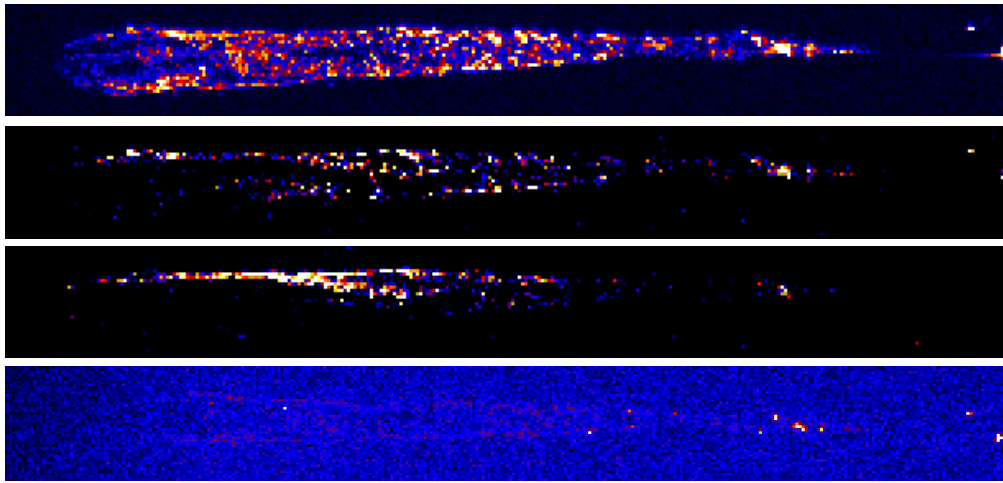
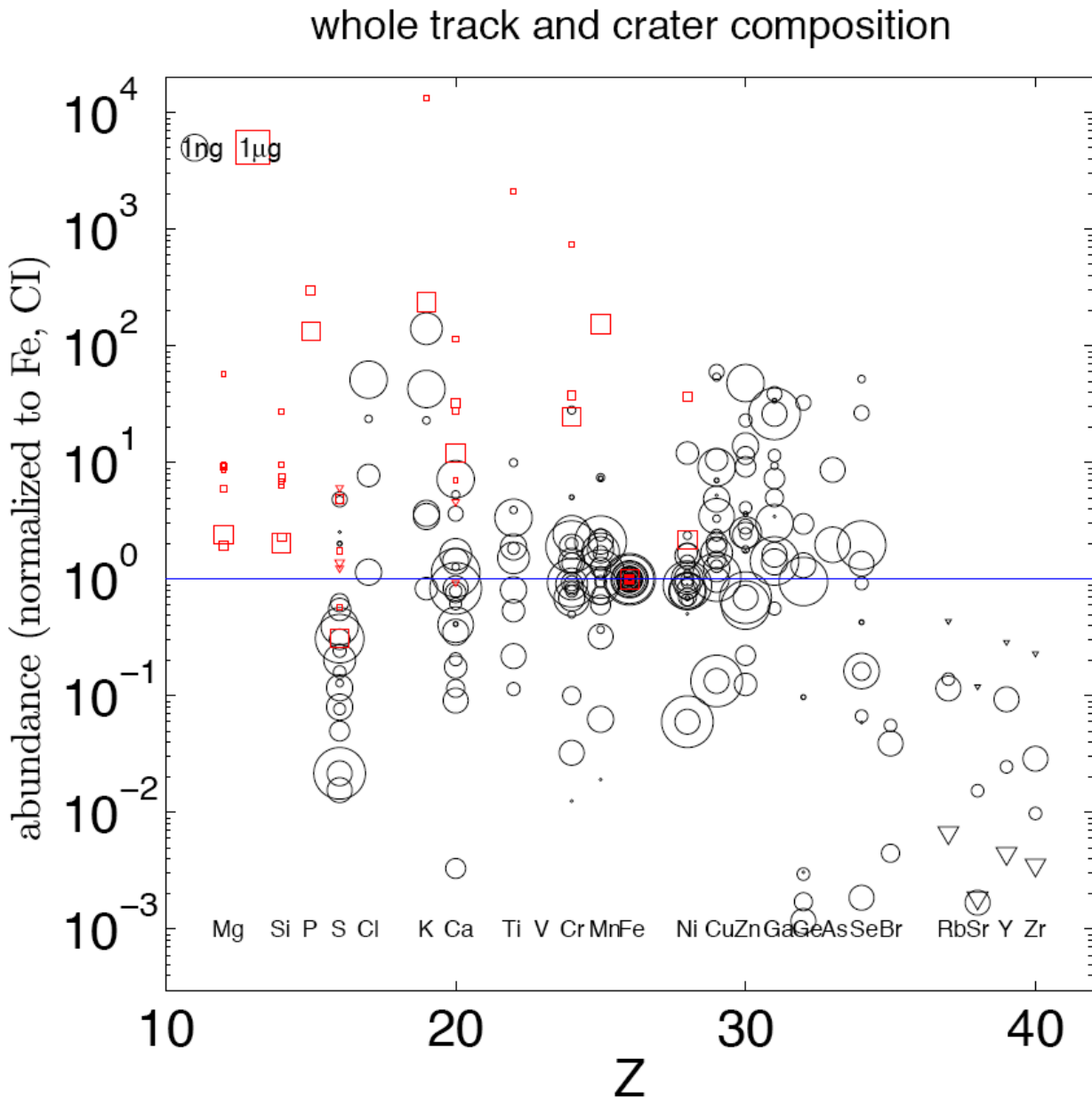


Figure 1: X-ray fluorescence analysis results obtained on Stardust Track 19, an 860 μm long track from aerogel cell C2115. Maps of the Fe, Ni, Zn, and Cr fluorescence intensities along Track 19, obtained at a step size of 3 μm /pixel, with a dwell time of 0.5 seconds/pixel, are shown. While the Fe is distributed along the track walls and in the terminal particle, the Ni is concentrated in the track walls, with little Ni in the terminal particle. Zn is distributed along only part of the track wall, while Cr is concentrated in the terminal particle. The maps were used to determine the coordinates of element hot-spots, which were subsequently analyzed for much longer times. The CI and Fe normalized element abundances for the terminal particle and the 19 most intense element hot-spots are plotted along with the “whole track average composition,” determined by adding the element abundances from 19 spot analyses along the track and the analysis of the terminal particle.

Figure 2: CI and Fe normalized whole track abundances in the 23 whole tracks and the 7 craters analyzed for chemical composition. The track data is denoted by circles radii? Whose diameters are proportional to the 1/3rd power of the mass of all the elements detected in the particle, while the crater data are shown as squares with side length proportional to the 1/3rd power of the particle mass inferred from the crater diameter. Because much larger masses were analyzed in the craters, there is a three order of magnitude difference in the scale size of the two symbols. The Fe and CI normalized data shows a high degree of variability from track to track, with most elements varying by two orders-of-magnitude or more.



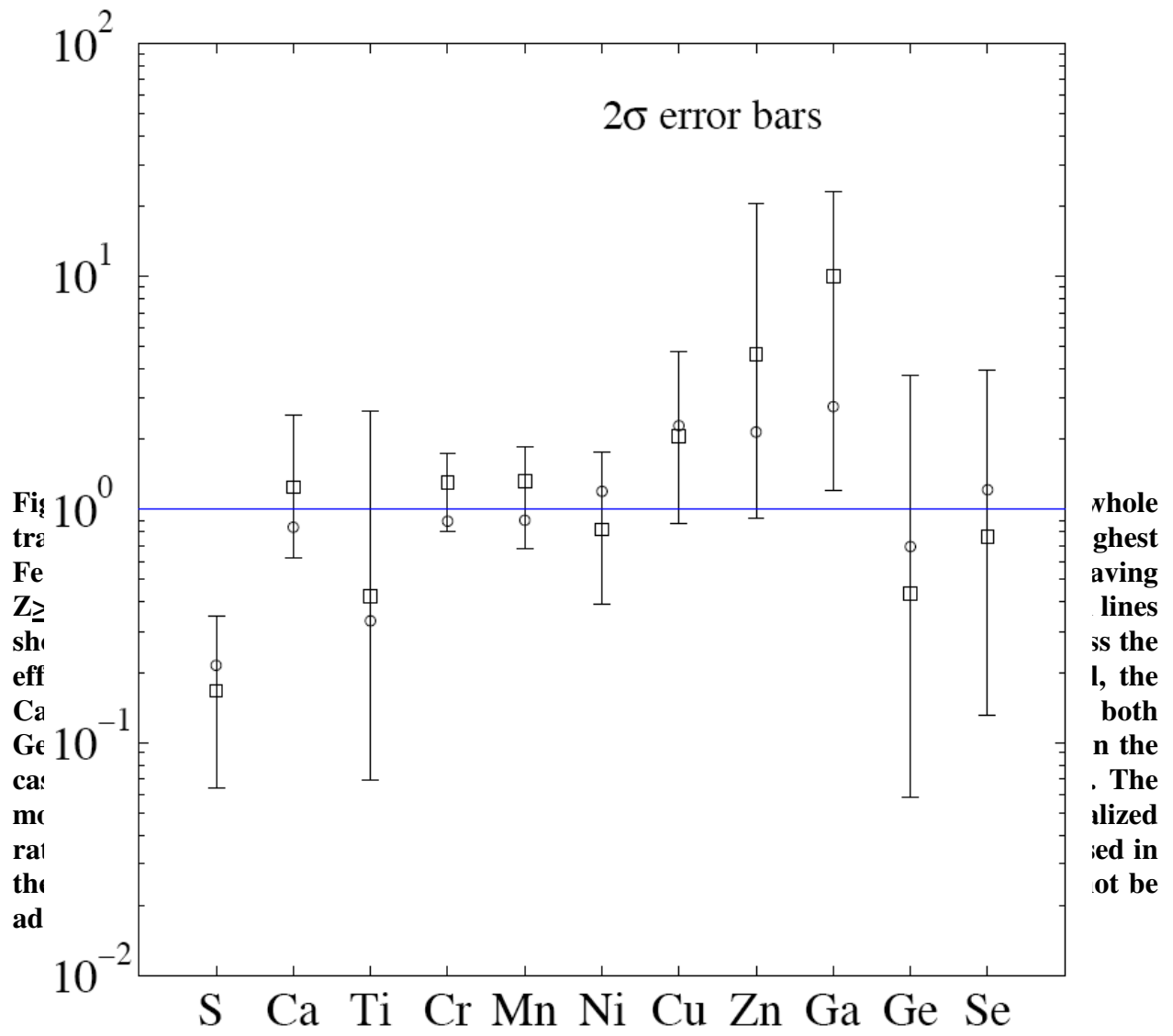


Figure 4: CI and Si normalized average composition determined by summing the 7 crater residue analyses, and by summing the same data set except for the largest crater. TOF-SIMS results for the 5 craters analyzed by that technique are also shown.

ATTACHED AS A PDF FILE. ANDREW CAN YOU INSERT IT IN THE WORD DOCUMENT?

SUPPLEMENTARY MATERIALS

Synchrotron X-Ray Microprobe Analysis

Synchrotron X-Ray Microprobes (SXRMs) employ high-intensity x-ray beams to excite x-ray fluorescence in a sample, and collect the x-ray spectrum allowing quantification of element abundances in the analysis spot. The energy of the x-ray analysis beam is high enough that it penetrates completely through an aerogel keystone, providing a relatively uniform excitation as a function of particle depth. The major limitation on element detection is the escape depth of the fluorescence x-rays, which limited these analyses to elements with an atomic number ≥ 16 (sulfur). XRMs do not suffer from the relatively large Bremsstrahlung background, which limits the sensitivity of electron beam analysis by the fluorescence technique. The high sensitivity of XRMs allows element detection down to tens of attograms in the analysis spot of some instruments. For the x-ray mapping of aerogel keystones, the element distribution was determined by raster-scanning the area containing the track, and generating element abundance maps.

The 6-month time period of the Stardust preliminary examination, coupled with the instrument time required to analyze the small amount of material distributed along each track in the Stardust aerogel, required an international collaboration to analyze a sufficient amount of material from the Stardust collection to establish a meaningful mean composition. The measurements that produced the results in Table A were performed at 5 synchrotrons: (FULL NAMES AND LOCATIONS PLEASE) SSRL, the Advanced Photon Source (Argonne National Laboratory, Argonne, IL USA), the National Synchrotron Light Source (Brookhaven National Laboratory, Upton, NY USA), ESRF, and Spring 8, with additional data being obtained at the ALS. The XRMs at these synchrotrons differ in their analysis conditions and their analytical capabilities. The individual instruments employed in this project are described below.

Prior to the Stardust landing, Allende powder and powder from a microprobe standard “unknown” were shot into aerogel cells. Tracks containing both materials were prepared as aerogel keystones, and provided to each group participating in the SXRm analysis of Stardust samples during the Preliminary Examination. The Allende samples were used to provide an indication of the elements each instrument can detect in a chondritic sample while the “unknown” was used to insure consistency in analyses among the laboratories. Even for a relatively strong material like Allende, a considerable amount of material was deposited along the entry track, so we anticipated that in order to determine the chemical compositions of the Wild 2 particles it would be necessary to integrate the chemical composition over the material along the entry track, rather than concentrating on the analysis of the terminal particles.

ESRF

The ESRF ID22 and ID21 beamlines, dedicated to high respectively low energy microspectroscopy were used for the analyses. Initially, whole track analyses were done on ID22, at 13 keV incident energy, with either $2 \times 2 \mu\text{m}^2$ or $2 \times 4 \mu\text{m}^2$ resolution (for the very large maps) and 1E11 ph/s in the beamspot. A 13 elements Gresham Si(Li) detector set at 90° to the beam direction in the horizontal plane was used for the fluorescence detection and two PIN diodes in transmission for beam intensity before/after the sample monitoring. Finally, high resolution maps were taken of $20 \times 20 \mu\text{m}^2$ areas around the terminal particles, with $1 \times 1 \mu\text{m}^2$ resolution and 1 sec/point acquisitions. Beam was monochromatized by a Si 111 flat double crystal Kohzu monochromator and focused by a remote controlled double bent Kirkpatrick-Baez mirror device. For some keystones, XANES around the respective K edges of Fe or S was performed, on the ID21, using a Si 111 monochromator. FZP lenses were used there to produce square beamspots of 1 respectively $0.3 \mu\text{m}$ for the Fe respectively S edges with about 1E9 ph/s. A thin Kapton foil coupled to a Si PIN diode was used to monitor the incident beam intensity and a high resolution HpGe detector for fluorescence.

APS and NSLS

X-ray fluorescence (XRF) maps and spot XRF analyses were measured using the undulator-based microprobe at Sector 13 (GeoSoilEnviroCARS) at the Advanced Photon Source (APS), Argonne National Laboratory and bending-magnet based microprobe at beamline X26A at the National Synchrotron Light Source (NSLS), Brookhaven National Laboratory (Sutton et al. 2002). Both instruments used a Si (111) monochromator and Kirkpatrick-Baez microfocusing mirrors (KB; Kirkpatrick and Baez, 1948; Eng et al. 1995, 1998; Yang et al. 1995). The KB system consists of two mirrors (100 mm length) in tandem, one oriented horizontally and one oriented vertically. Each mirror, a highly polished, flat, single crystal of silicon coated with several hundred Å of Rh, is dynamically bent to an elliptical shape using a mechanical bender. A 300 x 300 µm x-ray beam incident on the mirror pair is focused by reflection to ~3 x 3 µm (APS) and ~5 x 8 µm (NSLS). The incident beam energies were 16.5 and 23 keV (NSLS and APS, respectively). XRF spectra were collected using a Vortex-EX silicon drift detector using digital signal processing electronics with energy resolution of ~130 eV. Maps were acquired by rastering the sample in the x-ray beam with 3 and 5 µm steps for the APS and NSLS, respectively. Dwell times for maps were between 0.5-1 second and 3-17 seconds (APS and NSLS, respectively). Total mapping times were typically several hours per track. Full XRF spectra were saved at each analysis pixel. In addition, longer dwell spot XRF analyses (typically 5-16 mins) were obtained on spots along the track with high count rate (typically high Fe K count rate) in order to increase the number of detectable elements.

Spectra were processed in two ways. In some cases (C2009,20,77; C2086,1,65,0,0), all spectra in a map were summed to produce a whole-track spectrum. A portion of the map “off-track” was then summed to produce an aerogel background spectrum. The whole-track and aerogel spectra were then subtracted using total pixels summed in each for normalization. The net spectrum was then fit using a Gaussian based routine and the net peak areas converted to masses using comparable measurements on SRM thin film standards 1832/1833. NRLXRF (Criss 1978) was used to extrapolate sensitivities to elements not present in the SRMs.

In other cases (C115, Tracks 19-22; C2044 Tracks 7, 12 and Big Track), the long dwell time spectra on “hot-spots” were fit individually and elemental masses computed for each as above using “off-track” aerogel analyses for background subtraction. These elemental masses were then summed and scaled to produce whole-track masses. The scaling factor, required because only a fraction of the total track was analyzed, was taken to be the ratio of the Fe mass in the summed analyses and that in the map. These factors were typically in the 2-5 range but were as high as 21 in a highly dispersed track (C115 Track 19). The use of this scaling factor assumes that the average composition of the analyzed material is the same as that for all the material in the track. This assumption will be most valid for tracks produced by fine-grained aggregates and less valid for those dominated by large mineral grains.

For elements greater than Ca where self- and aerogel absorption is negligible, the precisions in the masses for the whole tracks (integrated map or sum of particle analyses) are better than 20%. There are at least 1000 counts in these integrated spectra for all elements reported corresponding to a <10% statistical uncertainty. The SRM thin film standards used for mass determinations have uncertainties of between 3 and 10%. Thus, the mass precisions are better than 20%. The error in the Fe masses are actually near 3% (counting statistics negligible, dominated by standard uncertainty), i.e., small compared to the uncertainties in the other masses. So, the Fe normalized abundance uncertainties are about 20%.

The GeoSoilEnviroCARS microprobe At the Advanced Photon Source is supported by the US National Science Foundation – Earth Sciences (NSF EAR-0217473) and US Department of Energy- Geosciences Research Program (DOE DE-FG02-94ER14466). The X26A microprobe at the National Synchrotron Light Source is supported in part by the US Department of Energy – Geosciences Research Program (DOE DE-FG02-92ER14244)

SSRL

The hard x-ray scanning microprobe at the Stanford Synchrotron Radiation Laboratory (SSRL), Stanford Linear Accelerator Center is an endstation of wiggler Beam Line 6-2 and has a 2 micron minimum beam size with 10^9 photons/second (ph/s). X-ray fluorescence (XRF) maps and spot analyses were performed using 14 keV x-rays from a Si (111) monochromator defined by virtual source slits and focused by Kirkpatrick-Baez optics. For whole track mapping, focused spot size was either 15 x 19 microns or 6 x 16 microns for efficient mapping with 2 to 5×10^{10} ph/s in the beam spot. The sample was translated in the beam in steps matched to spot size with dwell times of at least 30 seconds/pixel and as much as 500 seconds/pixel for a small track. Full fluorescence spectra were collected at each pixel. Terminal particles and other particles along tracks were located primarily by high Fe count rate. For particle spot analyses and a few high resolution maps of terminal regions, the focused spot size was reduced to 3.5 x 4.5 microns with 3×10^9 ph/s in the beam spot. Long count time spectra on particles were typically 2000 seconds up to 5000 seconds; however, for consistency, terminal particle data reported here were isolated from whole track maps. A Si(Li) detector with ~150 eV resolution collected the fluorescent x-rays in a geometry perpendicular to the incident beam in the plane of the storage ring. PIN diodes provided pre- and post-sample intensity measurements.

XRF map spectra were processed as follows: In mapping the track, pixels extending outside the comet particle track were also measured. The portion of the map without cometary material provided the background contribution from the aerogel. Spectra were fit using PyMca, a program developed by Dr. Armando Sole at the European Synchrotron Radiation Facility (ESRF). Whole track mass was derived from the difference between the summed track spectra containing cometary material and the averaged background concentration for the same number of pixels. Two types of reference standards were used: a thin (200 nm) Fe film was used as an absolute reference standard and a USGS basaltic glass microprobe standard (NKT-1G) was used to determine the energy-dependent correlation for elements above and below Fe. Mass precisions are generally 20% or better for elements above Ca. Statistical uncertainty is <10% for all elements reported in whole track data. For terminal particles, due to reduced total counts, the statistical error is as high as 17% in low-abundance elements, Ga and Se. Uncertainties in the thin film standard compositions are <1% for elements referenced. Error in Fe mass is dominated by uncertainty in the standard thickness and is at most a few percent.

The Stanford Synchrotron Radiation Laboratory is a national user facility operated by Stanford University on behalf of the U.S. Department of Energy, Office of Basic Energy Sciences.

Spring 8

We analyzed tracks in four kestones at SPring 8 by SXRF using a 15 KeV monochromated X-ray beam, with an exposure time of mostly 2000 sec and sometime 1000 sec. The length of tracks is up to 3 mm. We analyzed entire tracks using a broad beam up to 400 x 260 micron in size. By this analysis we obtained total XRF counts of elements in the tracks plus particles. After that, the beam was narrowed down using two sets of slits and only particles were analyzed

using 60 x 60 micron beam, in order to obtain XRF counts of elements sited in particles. Then, we determined XRF counts of elements only in tracks by subtracting XRF counts of a particle from those of a track plus the particle in the corresponding area.

All elements were collected for blank that was obtained by measuring portions consisting of only aerogel. Five particles of Orgueil CI chondrite with a diameter of about 150 microns were analyzed, in order to obtain XRF counts of elements with solar abundance. By averaging the five Orgueil results and normalizing to solar abundance, we obtained the elemental abundance of tracks and particles in kestones.

Conversion of XRF counts to weights of elements was done in the following procedures. For each keystone, we measured a portion of aerogel where no tracks and no particles are present. We calculated a weight of element Si in the analyzed portion was obtained from the density and the volume of the aerogel where the beam was passing through. We obtained sensitivity of Si (S(Si)) in our analysis;

$$S(\text{Si}) = C(\text{Si})/W(\text{Si}) \text{ [cps/g]} \text{ -----(1)}$$

Where C(Si) is XRF counts of Si and W(Si) is weight of Si.

By averaging the results of analysis of five Orgueil standard particles and by normalizing to solar abundance, we obtained the ratio of the sensitivity of a element X to Si;

$$F = S(X)/S(\text{Si}) = (C(X)/W(X))/(C(\text{Si})/W(\text{Si})) = (C(X)/C(\text{Si}))/ (W(X)/W(\text{Si})) \text{ -----(2)}$$

F is obtained from Orgueil analysis; $F = (C(X)/C(\text{Si}))_{\text{Orgueil}} / (W(X)/W(\text{Si}))_{\text{Orgueil}}$. Because we know $(C(X)/C(\text{Si}))_{\text{Orgueil}}$ from measurement and $(W(X)/W(\text{Si}))_{\text{Orgueil}}$ from literature data of solar abundance. Also from equation (2),

$$F = (C(X)/W(X))/(C(\text{Si})/W(\text{Si})) = \text{----- (3)}$$

From equation (1) and (3) we obtain

$$W(X) = C(X)/(F S(\text{Si})) \text{ ----- (4)}$$

S(Si) is obtained from measurements of aerogels, F from measurements of Orgueil particles, and C(X) from measurements of stardust particles or tracks. Then we can obtain W(X), weight of element X.

Error for W(X) was estimated by applying error propagation for the equation (4). Error for W(X) is propagated from errors of C(X), F, and S(Si), and the three parameters are independent each other, because they are obtained from analysis of three different material: C(X) is obtained from stardust tracks or particles, F from five particles of Orgueil. Error for W(X) was obtained from the following equation.

$$(\sigma W(X))^2 = \left(\frac{\partial W(X)}{\partial C(X)} \right)^2 (\sigma C(X))^2 + \left(\frac{\partial W(X)}{\partial F} \right)^2 (\sigma F)^2 + \left(\frac{\partial W(X)}{\partial S(\text{Si})} \right)^2 (\sigma S(\text{Si}))^2$$

$$= \left(\frac{\sigma C(X)}{FS(Si)} \right)^2 + \left(\frac{C(X)\sigma F}{S(Si)F^2} \right)^2 + \left(\frac{C(X)\sigma S(Si)}{FS(Si)^2} \right)^2$$

Complications in the Analysis of Particles in Aerogel

For the lightest elements we analyzed, S and, to a lesser extent Ca, a correction for the absorption of the fluorescence x-rays due to the aerogel on the path from the analyzed atom to the detector is required. The structure of the Stardust aerogel, a graduated density aerogel having very low density near the surface, about 20 mg/cc aerogel farther down, and 50 mg/cc aerogel near the bottom (optimized to produce minimal deceleration for the smallest particles, which are stopped in the upper layer, but to stop particles up to >100 μm in diameter within the 3 cm thickness) complicates this correction, since the density of the aerogel varies along the track in a manner that has not been well-characterized, and may differ from cell to cell. In addition, since some of the material extracted from tracks for examination consists of comet material distributed inside pieces of compressed or melted aerogel, sometimes large enough to significantly attenuate S fluorescence x-rays, detailed corrections for absorption have not been possible.

A second complication arises from the trace contamination of the aerogel itself. An ICPMS analysis of a cell of Stardust aerogel (TSOU PAPER) showed trace quantities of most stable elements were present in the aerogel.

SXRM analysis of part of a Stardust a flight aerogel cell (C2054, 8) that was free of particle tracks was measured using an SXRM. The analyzed volume of this cell contained trace quantities of Ca (7.5 ppm), Fe (1.0 ppm), Ni (0.4 ppm), Cu (0.8 ppm), and Zn (3.1 ppm), frequently localized in hot-spots.

These contamination hot-spots complicate the background subtraction of the trace contaminants. Figure F shows a map of the spatial distribution of Fe and Ca in cell C2115. The Fe marks the path of the particle, while Ca is found in hot-spots throughout the aerogel. When a Ca hot-spot is coincident with the particle track, the hot-spot cannot be unambiguously identified as either contamination or comet material. Figure F shows a map obtained on a half-cell, which is 2 cm thick, thus it has many more Ca hot-spots along an analysis beam path than in a 200 to 300 μm thick keystone. But, even in the the keystones, which were analyzed to obtain the data reported in this paper, chance overlaps between contamination and the particle track can occur. Backgrounds were subtracted by analyzing comparable areas of track and adjacent, non-track aerogel, but the heterogeneous distribution of contamination in the aerogel leaves uncertainty in these background corrections.

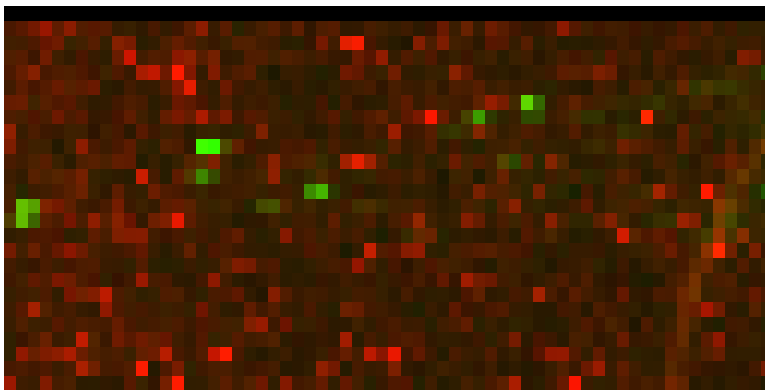
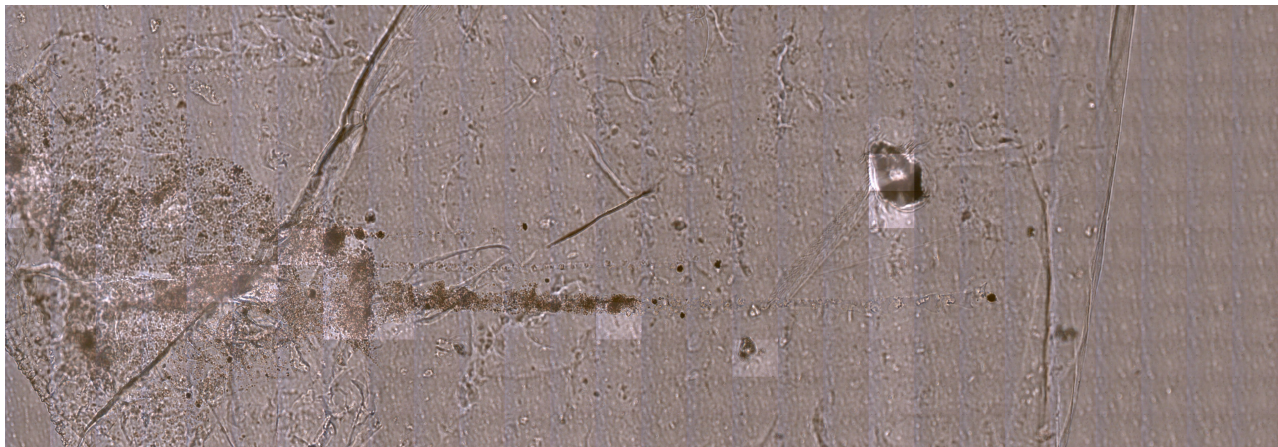


Figure F: Map of the x-ray fluorescence intensity from Fe (green) and Ca (red) in an area centered on a particle track (identified by the Fe) in Stardust aerogel cell C2115. This map was obtained on a half-cell of 2 cm thickness, so there are many more Ca hot-spots that we detect in a 200 to 300 μm thick keystone, but it illustrates the problem of correctly discriminating between a cometary Ca-rich fragment and aerogel contamination simply by its spatial association with the track.

Determination of the average composition of even a single track in the Stardust cometary collection is quite challenging. Figures G and H show two false-color SXRF maps of Track 77, shown in an optical microscope image in Figure F. Figure G is encoded with red proportional to the Fe concentration and blue proportional to the Ni concentration. In Figure H, red is proportional to the Fe concentration, green is proportional to the Mn concentration, and blue is proportional to the Cr concentration. There is an obvious fractionation between Fe and Ni in discrete particles and in the diffuse material distributed throughout the bulb of the track. It is thus necessary to integrate measurements over every part of the track. But determination of which parts of the map are in fact analyzing track material is not always unambiguous. Even among the discrete particles, there is a remarkable diversity in particle composition, and in particular in Fe content, even within this single impact. For example, the particle labelled 9d is rich in Mn and Cr, but shows no detectable Fe in this map. In the optical image of this track, 9d is the terminal particle of a track, so is unambiguously a component of the original projectile. Thus, it is critical to include spot 9d in the composition determination, but it is particularly difficult to determine its appropriate contribution to the average abundance in the hot-spot analysis technique (i.e., how many Fe hot-spots must be added to one Mn hot spot).

Figure F: Optical microscope image of Tarack 77.



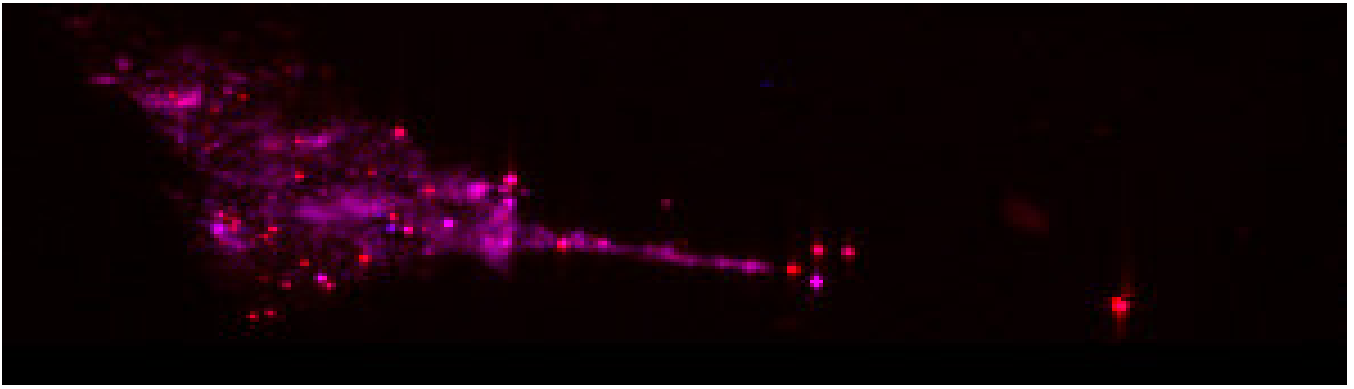


Figure G: False-color map of the Fe (red) and Ni (green) distribution along Track 77, showing that in many areas Ni and Fe are fractionated from one another.

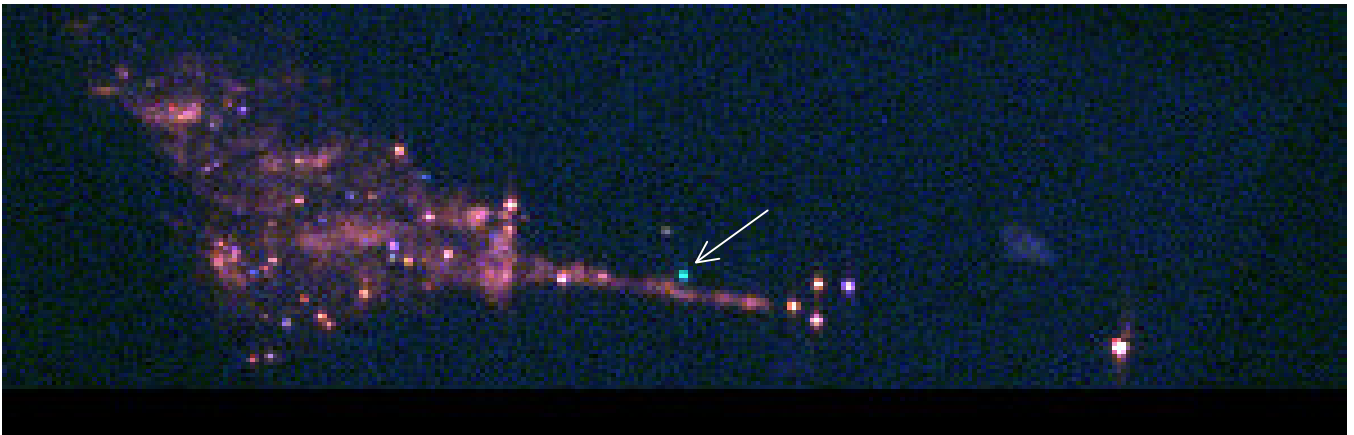


Figure H: False-color image of the same track area in Figure G, showing the Fe (red), Mn (green), and Cr (blue). Spot 9 is rich in Mn and Cr, but has no detectable Fe.

Comparison of the Hot-Spot and Track Mapping Techniques

One objective of the Preliminary Examination of the Stardust samples was to investigate a variety of techniques for analysis of particles collected using aerogel capture. Because the amount of SXRМ time available for the Stardust Preliminary Examination was limited, and our first analyses demonstrated that each track was significantly different from the next one, it was necessary to devise strategies that allowed the analysis of enough tracks to obtain a convergent average composition. The limit on available SXRМ analysis time precluded us from performing the analyses in the ideal mode, using a sufficient dwell time at each pixel in the map to obtain a spectrum of sufficient quality to unequivocally identify minor elements above the instrumental background. The “whole track” average compositions reported in this paper were determined using two significantly different analytical approaches. One set of tracks was analyzed by mapping the sample using relatively short dwell times per pixel, detecting only elements with $Z \geq 16$ that were present at relatively high concentrations in an analysis pixel. The element hot-spots identified by this technique were subsequently analyzed for significantly longer times, and the results from the spot analyses were summed to obtain an average composition. The longer dwell time on the hot-spots allowed the detection of trace elements that could not be seen in the maps, but this technique assumes that the composition of the hot-spots reflects the composition of material distributed more finely throughout the track volume. A second technique, in which the mapping time was increased, and the average composition was determined by adding spectra from the area of the map provides more confidence that all of the material deposited by the particle has been included in the average, but suffers from a lower signal to noise that results from adding in many spectra that contain little elemental signal, resulting in fewer elements being detected than in the hot-spot analysis of the same track.

We compared these two basic methods to look for systematic differences. Since only one track was analyzed by different laboratories, one employing the hot-spot technique and the other the track mapping technique, the comparison is done with different particles in the data set. Figures X and Y are the equivalent of Figures 2 and 3 of the text, 2 and 3, but here the data has been separated according to the analytical method and 1-sigma error bars are shown rather than the 2-sigma error bars shown in Figures 2 and 3 of the paper. No systematic difference is evident between the two methods. However, a systematic effect smaller than the statistical error bars cannot be ruled out by this comparison.

whole track and crater composition

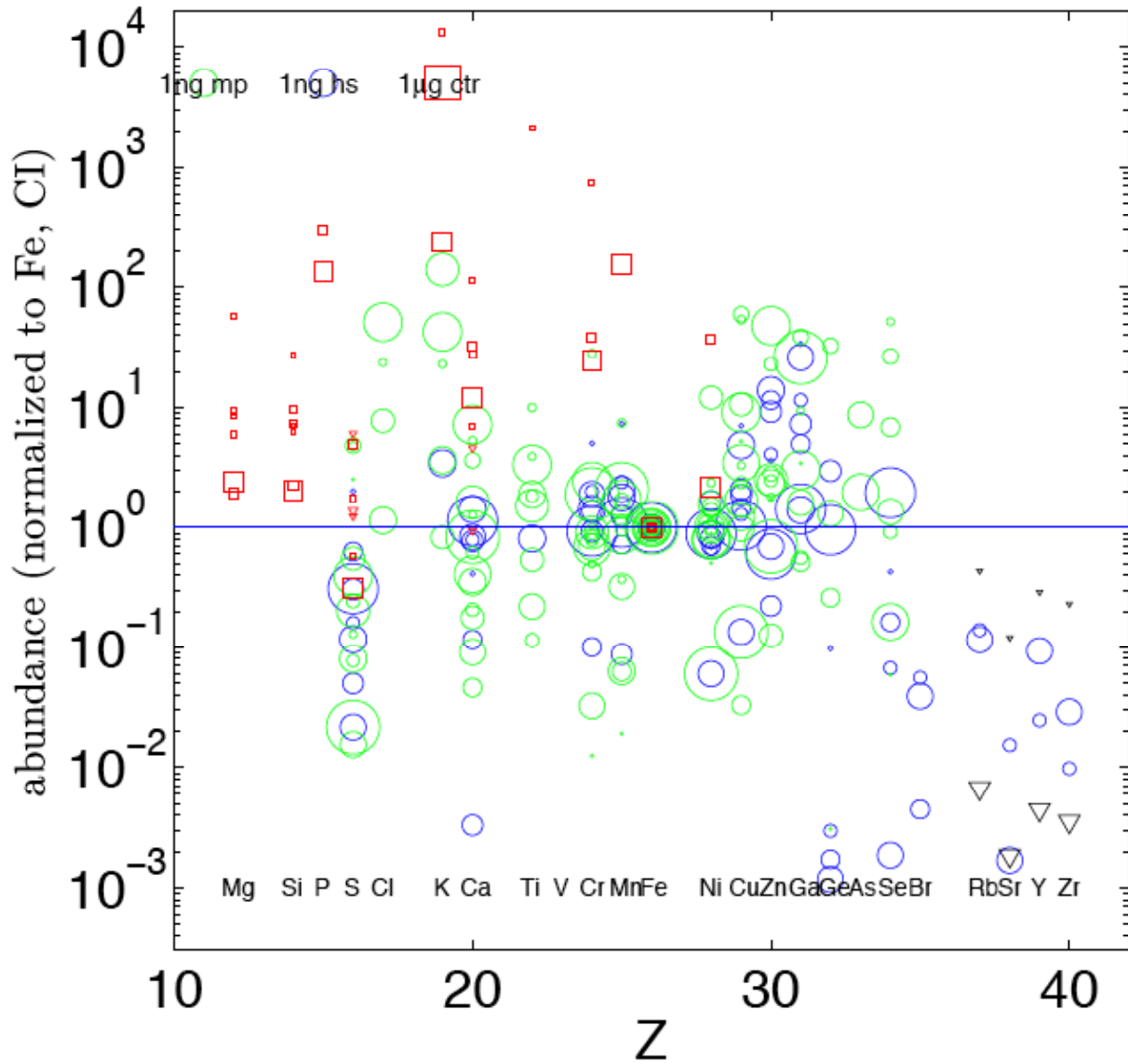


Figure X: “Whole track” compositions of 9 tracks analyzed by the hot-spot technique (shown as blue circles) and 15 tracks analyzed by the track mapping technique (shown as green circles). One track, analyzed by both techniques, is shown twice.

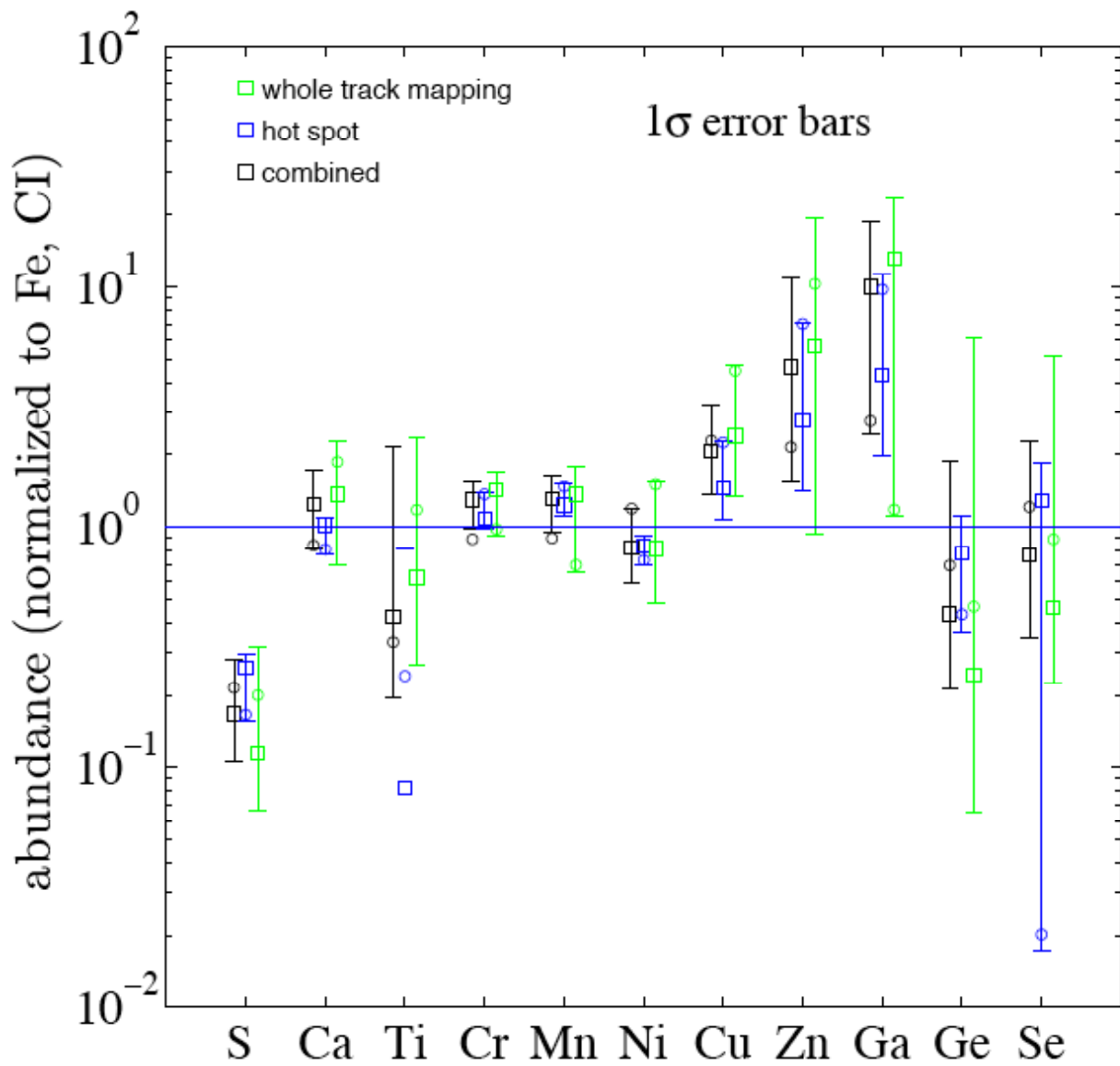
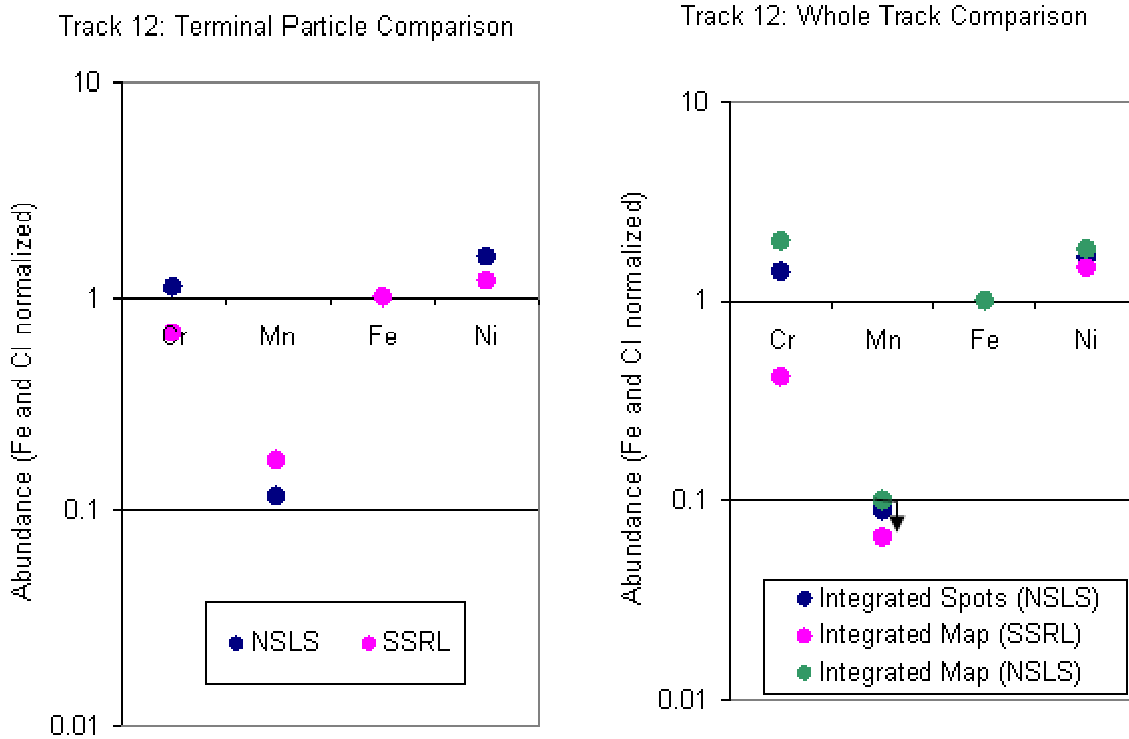


Figure Y: Comparison of the mean compositions of the 9 tracks analyzed by the hot-spot technique (shown in blue), the track mapping technique (shown in green), and the combined data (shown in black), with 1-sigma error bars generated by the Monte Carlo technique (described below) on the individual data sets.

Further intercomparisons between the two techniques have been performed on Track 12 and Teack 19

Track 12 Analyses by Two X-ray Microprobes: Track 12 was analyzed by the NSLS and SSRL x-ray microprobes. The left plot below shows a comparison of the Fe and CI normalized abundances for the terminal particle. The agreement for Mn and Ni is at the 30% level and the Cr difference is 70%. The second plot shows the whole track results with three datasets shown. “Integrated Spots (NSLS)” are the abundances determined by summing the elemental masses for hot spots in the track map. “Integrated Map (NSLS)” and “Integrated Map (SSRL)” are the abundances determined by integrating the spectra at each pixel of each track map (upper limit indicated by arrow). All three datasets are consistent at the 40% level with the exception of Cr where there is about a factor of 3 difference between the NSLS (both methods) and the SSRL data.



Track 19 Analysis by Spot Integration and Map Integration: The plot below for the abundances in Track 19 (analyzed at the APS) shows a comparison of results using two different methods of “whole track” analysis: the “integrated spot” and “integrated map” methods. The results are consistent at the 25% level for Mn, Ni and Zn. Cr and Cu show differences of about a factor of two. Differences may result from the hot-spot technique analyzing a smaller fraction of the total material than the mapping method. These results together with those for Track 12 above provide evidence for the level of inaccuracies associated with integrating a subset of the track material.

Track 19 Whole Track Comparison

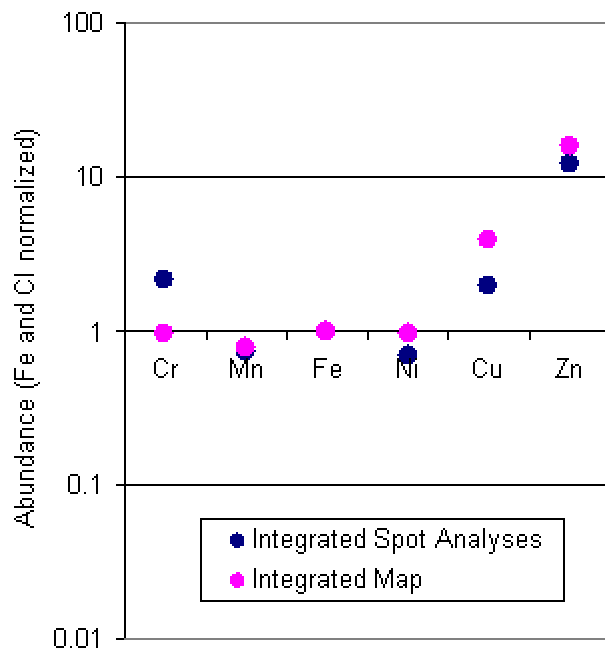


TABLE OF SXR ANALYSES OF TRACKS GOES HERE

TOF-SIMS of Bulb Slices

Here are the data from the track measurements that were performed in Washington DC and in Münster. These were both samples from the very same track (C2115,21). We had two slices from one side of the bulb. The track was first dissected lengthwise. Then, one half was sectioned into many slices. Slice 2 went to the Smithsonian, Slice 6 to Münster. Consequently, each group analyzed only a small amount of material compared to the entire track, and each group analyzed a different part of the track. Therefore, it is no surprise that our results are not the same. However, we both used the same principles of data reduction. We made blank correction assuming that the Si/Fe in the residue is CI-chondritic. The surplus of Si is attributed to the blank. The composition of the blanks was determined from regions in the aerogel surrounding the respective tracks. Finally, we discarded those data points where the blank is higher than 50 % of the entire signal or where the blank is extremely heterogeneous and therefore a clear attribution of the measured signal to cometary material cannot be made.

The resulting data are summarized in the following table that you should use for plotting the data. Errors are 1σ statistical errors resulting from counting statistics and blank correction. Data in red have high statistical error ($>1/3$). We therefore leave it up to you, George, if you want to plot these data points.

	Slice 2 (Smithsonian)		Slice 6 (Münster)	
	Fe- and CI-normalized	error	Fe- and CI-normalized	error
Na			1.252	0.060
Mg	0.870	0.017	0.525	0.011
Al	1.277	0.073	0.686	0.044
Ca	0.192	0.025	0.202	0.022
Ti	1.573	0.699		
Cr	0.959	0.197	0.850	0.167
Mn	0.958	0.345	0.857	0.505
Fe	1.000	0.036	1.000	0.029
Co	1.102	0.927	1.946	1.125
Ni	3.525	0.436	2.556	0.406

Crater SEM-EDX

The chemical composition of the residue in each of the 7 large craters in the Al-foil was determined using an Oxford Instruments INCA energy dispersive X-ray (EDX) spectrometer. The analyses were performed at 20 keV and 2 nA. The exposed surfaces were rough and were not carbon coated, so the matrix corrections are approximate, these effects are described in detail by Kearsley et al. (2006b). Wherever possible the sample was tilted to allow electron beam incidence perpendicular to the residue surface (Tilt), which permits the most appropriate matrix correction. The X-ray spectra from which the quantitative data are derived were taken from large patches of residues in the crater floor, most using the tilted orientation, with relative count rates suggesting that they are of close to micron-scale thickness. The element abundances were calculated by comparison to the suite of silicate, oxide and sulfide standards at the Natural History Museum, processed with an extended Pichou and Pouchoir (XPP) correction, then normalized to 100%, but Al was excluded from the subsequent calculations because of the ubiquitous excitation of the Al-foil substrate. All analyses were performed in high vacuum except the analysis of

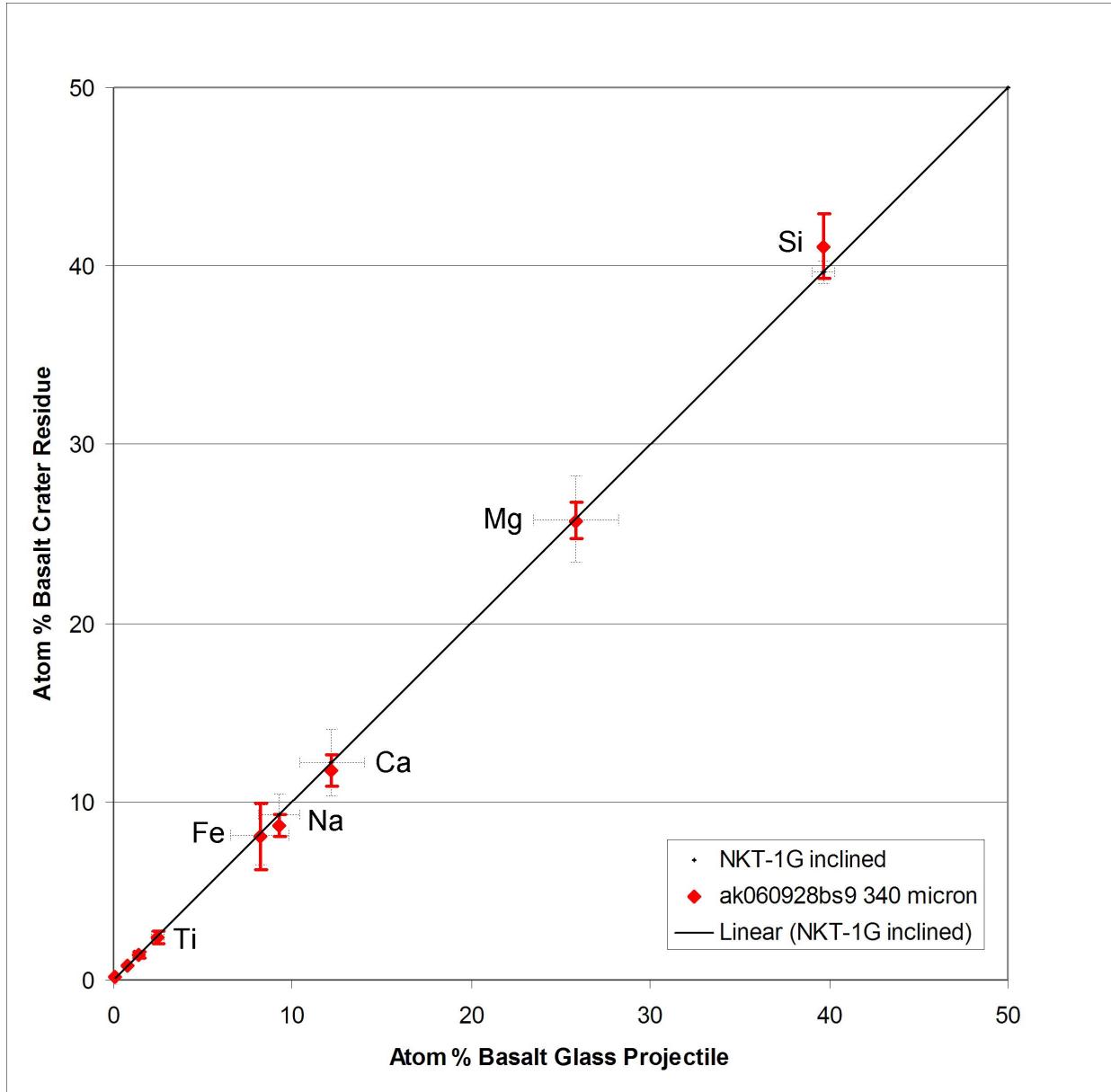
C2107W,1, which was performed at low vacuum (30 Pa). All element abundances are shown in Table (the SEM-EDX data for the large craters) as wt-% oxides, although S is likely to be present as a sulfide (as observed in C2029W,1). A measure of the level of precision and comparability to pre-impact composition that can be expected for the Stardust crater residue analyses by SEM-EDX is seen in figure YY, a plot showing the typical dispersion (grey error bars) of analyses expressed as atomic ratios in a comparison between light gas gun residues of basalt impact and a suite of rough projectile surfaces (of very well known composition). (A copy of this figure is attached, do you want me to spell out the relative error bar sizes in the text too, or let them be read from the plot?).

Anton: Yes, a sentence stating the errors would probably help the readers

Table 2. Bulk residue composition in Stardust foil craters of greater than 50 microns diameter. All analyses are averages or area integrals, performed using an Oxford Instruments INCA energy dispersive X-ray spectrometer using 20kV and 2nA. Surfaces were rough and with no carbon coat, matrix corrections are therefore approximate. Aluminium was excluded from the fitting routine due to ubiquitous excitation of the metal substrate (not determined = nd), and results were normalised to 100%. Wherever possible the sample was tilted to allow electron beam incidence perpendicular to the residue surface (Tilt), giving best matrix corrections. All analyses at high vacuum except C2107W,1 (low vacuum LV, 30 Pa). All determinations are shown as wt% oxides, although S is likely to be as sulphide, as observed in C2029W,1. Determinations of less than 3 times background variation are listed as ‘below detection limit’ (Bdl). If detected in more than one determination for the crater, the element is listed as ‘trace’. The ratio of the sum of the divalent cations (minus iron for FeS) to Silicon is shown as ‘[Div]/Si’. Mg: (Fe-S) ratio is intended to show ratio in silicate, with Fe subtracted for inclusion in FeS. Probable mineralogy is based upon evidence of stoichiometric relations typical of a particular mineral family: ‘Ol’ is olivine; ‘Px’ pyroxene; ‘Su’ sulphide; ‘non-stoich’ residue may be ‘mafic’ (Ma) and/or ‘alkaline’ (Ak) rich..

Crater	C2009N,1	C2029W,1	C2086W,1	C2086N,1	C2091N,1	C2107W,1	C2118N,1
Morphology	Bowl	Field	Bowl?	Bowl	Field?	Bowl	Bowl
Diameter (microns)	64	167 x 133 irregular	238	57	62	85	68
Method	Normal EDS	Normal EDS	Tilt EDS	Tilt EDS	Normal EDS	Tilt EDS LV	Tilt EDS
Oxide wt %	Point analyses	Whole area integrated	Small area integrated	Point analyses	Point analyses	Point analyses	Point analyses
SiO ₂	47.4	26.0	35.7	41.5	46.6	49.0	54.3
TiO ₂	<	0.1	<	<	<		<
Al ₂ O ₃	nd	nd	Nd	nd	nd	nd	nd
MgO	38.0	33.4	26.9	55.4	40.2	38.3	21.4
Cr ₂ O ₃	3.1	0.2	0.2	0.5	trace	trace	1.2
MnO	<	0.4	0.5	<	<	trace	trace
FeO	10.6	20.1	31.5	2.7	13.2	11.8	10.1
NiO	<	2.4	0.2	<	<	<	<
Na ₂ O	<	0.2	2.0	<	<	<	6.1
K ₂ O	<	<	trace	<	<	<	1.1
CaO	<	1.1	1.0	<	<	0.9	3.1
P ₂ O ₅	<	<	0.2	<	<	<	0.3
SO ₃	0.7	16.1	1.6	<	<	trace	3.0
Comment	7 points, Cr variable from below detection.	Much Fe and S as Sulfide, Al with Na in Px?	2 mixed phases. K ₂ O reaches 0.6 wt%.	12 points across crater floor	5 points on crater top lip.	10 points on crater floor. Also trace Cl.	Also trace Cl
[Div]/Si	1.5	1.0 (Px)	2.0 (Ol)	2.0 (Ol)	1.6	1.4	0.8
Mg:(Fe-S)	6.5	35.8 (Px)	2.1 (Ol)	36.5 (Ol)	6.4	5.8	5.2
Probable mineralogy	Unknown	Px, Su, and non-stoich Ma	Ol (Fo 65) + non-stoich Ak	Ol (Fo 97)	Unknown	Unknown	Non-stoich Ma/Ak
Estimated mass (ng)	3.4	17	178	3.1	3.1	8.0	4.2

Figure YY: Need Caption.



To quantify the effect of element loss during the production of impact residue, a variety of projectiles were shot onto Stardust Al1100 foil in the light gas gun at the University of Kent at close to the Stardust encounter velocity of 6.1 km/s (Kearsley et al., 2006b). Experiments with pyrrhotite (iron sulfide) projectiles demonstrated that there is loss of sulfur during impact. SEM-EDX analyses of residue on the rough floor of craters of less than 10 μm diameter gave poor data due to substantial matrix correction problems, but analytical transmission electron microscopy (AEM) at Lawrence Livermore National Laboratory on a focused ion beam section through a 12 μm diameter crater showed reduction in sulfur from 39% to 27% by weight in the residue. SEM-EDX of residue in craters of 150-200 microns diameter showed depletion from an original sulfur content of 39% by weight in the projectile, to 33% in the residue. Larger craters, >300 μm in diameter, contain coarse patches of residue (several μm thick) that are indistinguishable from the projectile in composition, although S is lost from thinner residues in the same crater.

Spectra were also obtained from the residue in craters produced by basalt glass projectiles (ca. 4% Na₂O). AEM data from sub-micron thickness basalt residue layers in small laboratory impact craters (less than 20 µm in diameter) showed localized depletion of Na (0-28% loss), Mg (0-9% loss), Si (10-14% loss) and Fe (0-10% loss), although almost all the AEM spectra have essentially the same composition as in the projectile, except for some loss of Si (Kearsley et al., 2006b). There is little change in any of these elements in craters >50 µm in diameter, except very minor Na loss (**bold red data in figure YY**) **this figure is attached.**

FIGURE

XX:

NEED

CAPTION

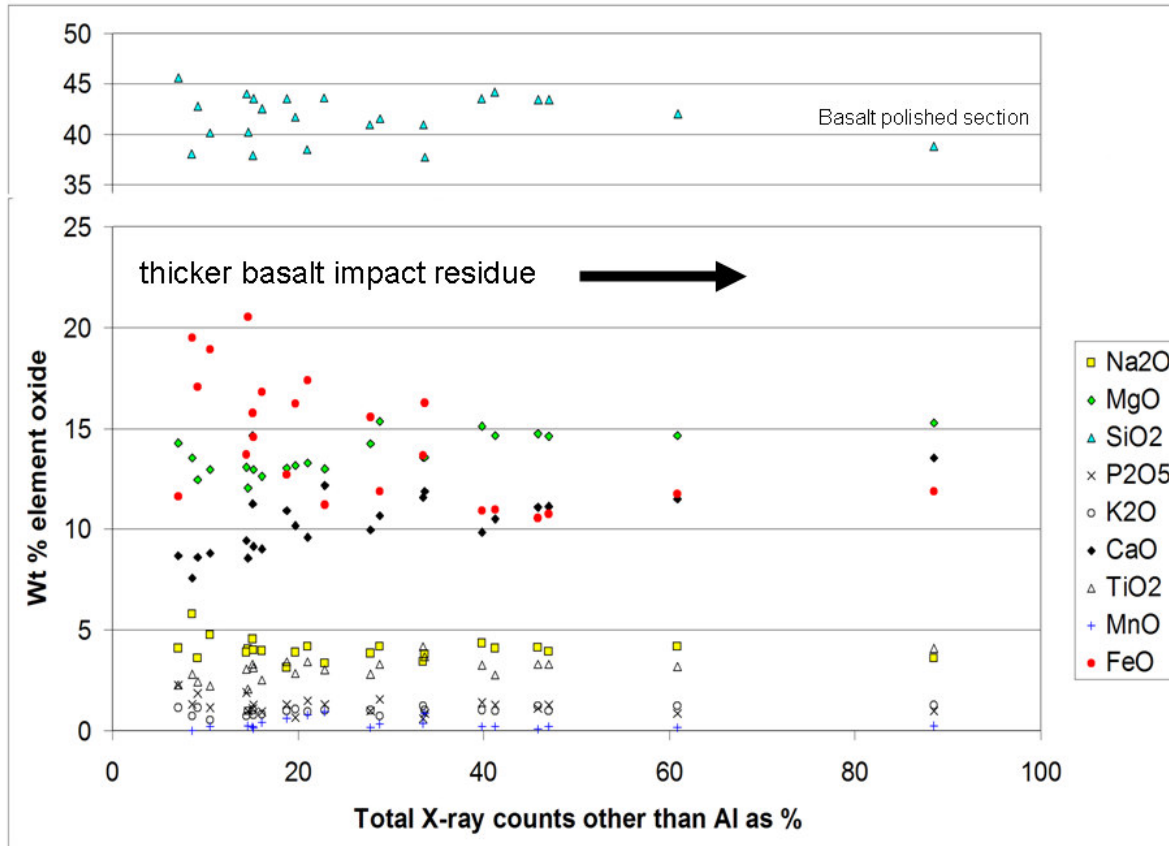


Figure XX shows SEM-EDX wt % oxide data from individual analyses of basalt residue (normalised and without Al₂O₃) plotted against a horizontal axis in which the % figure reflects the proportion of residue (as opposed to Al substrate) in the determination. The close match between crater data and the polished section analysis (89%, near right) suggests that there is no substantial problem due to either loss during impact or due to the analysis technique, although there is clearly dispersion of the Fe and Si figures in the thinner residues with lower residue wt%, probably due to a contribution from X-rays generated in inclusions within the underlying alloy. This implies that there is no substantial underestimation of the alkalis in the large crater EDS data, and certainly not so large as the apparent discrepancy between EDS and ToF-SIMS data might suggest. The spot EDX analyses all used a 50 second X-ray collection from a tightly focussed spot at 2nA current and 20kV accelerating voltage, which is a relatively gentle irradiation compared to conditions for wavelength dispersive X-ray analysis (ten times higher beam current and perhaps three times as long for acquisition), where it has been established that alkali migration does occur. X-ray maps which gave very short beam irradiation, less than 0.1 second per micron total, showed high alkali contents in two craters, but also that the alkalis were not distributed evenly at the micron

scale. In these craters analyses were taken from scanned areas, with much lower beam irradiation than spot analyses.

The chemical composition of the residue in each of these craters was determined using an Oxford Instruments INCA energy dispersive X-ray (EDX) spectrometer, using analysis conditions of 20 keV and 2 nA. The exposed surfaces were rough and were not carbon coated, so the matrix corrections are approximate. The element abundances were normalized to 100%, but Al was excluded from the fitting routine because of the ubiquitous excitation of the Al-foil substrate. Wherever possible the sample was tilted to allow electron beam incidence perpendicular to the residue surface (Tilt), which permits the best matrix correction. All analyses were performed in high vacuum except the analysis of C2107W,1, which was performed at low vacuum (30 Pa). All element abundances are shown as wt-% oxides, although S is likely to be present as a sulfide (as observed in C2029W,1).

To quantify the effect of element loss during the production of impact residue, a variety of projectiles were fired shot at ~6 km/s, close to the Stardust encounter velocity of 6.1 km/s, onto Stardust Al1100 foil. Analytical electron microscopy of small laboratory impact craters (less than 20 μm in diameter) show localized depletion of Na (0-28% loss), Mg (0-9% loss), Si (10-14% loss) and Fe (0-10% loss), but there is little loss of these elements in craters $>50 \mu\text{m}$ (Kearsley et al., 2006b). Light gas gun experiments with pyrrhotite (FeS) projectiles onto Stardust Al1100 foil demonstrate that there is loss of sulfur during impact. SEM-EDX analyses of residue on the floor of craters of less than 10 μm diameter gave poor data due to substantial matrix correction problems (Kearsley et al., 2006b). Larger craters, $>300 \mu\text{m}$ in diameter, contain coarse patches of residue (several μm thick) that are indistinguishable from the projectile in composition, although S is lost from thinner residues in the same crater. Craters of 150-200 microns diameter show depletion from an original sulfur content of 39% by weight in the projectile, to 33% in the residue. In a 12 μm diameter crater Kearsley et al. (2006) showed reduction in sulfur from 39% to 27% by weight in the residue. Thus, the chemical analysis of the residue in large craters is expected to provide a good sample of the composition of the dust that impacted the Stardust spacecraft.

The exposed surfaces of the crater residue were rough and they were not carbon coated, so the matrix corrections are approximate. Element abundances were normalized to 100%, but Al was excluded from the fitting routine because of the ubiquitous excitation of the Al-foil substrate. Wherever possible the sample was tilted to allow electron beam incidence perpendicular to the residue surface, which permits the best matrix correction.

The X-ray spectra from which the quantitative data are derived were taken from large patches of residues in the crater floor, most using the tilted orientation with relative count rates suggesting that they are of close to micron-scale thickness. Spectra were previously obtained from the residue in craters produced by basalt glass (ca. 4% Na₂O) projectiles shot in light-gas gun experiments. Data from sub-micron basalt residue layers in small craters is in the manuscript mentioned above, and for small craters, the analytical transmission electron microscope (AEM) data from Lawrence Livermore show some evidence for Na loss (up to 28% loss in the spectrum showing the most severe loss), although almost all the AEM spectra have essentially the same content as in the projectiles. I didn't put a lot of data on larger craters into that manuscript, however

I have now processed results from three 50 to 150 micron diameter LGG craters, which also show little variation (except the Fe signal from the alloy substrate). The determined Na content shows no sign of significant depletion from the analyses of the basalt projectile. The attached, unpublished, plot shows wt % oxides from individual analyses (normalised and without Al₂O₃) plotted against a horizontal axis in which the % figure reflects the proportion of residue (as opposed to Al substrate) in the determination. The close match between crater data and the polished section analysis (100%, at right) suggests that there is no big problem of either loss during impact or due to the analysis technique, although there is clearly dispersion of the Fe and Si figures in the thinner residues with lower residue wt%), probably due to X-rays generated from

inclusions in the underlying alloy. Because of these observations I am confident that there is no substantial underestimation of the alkalis in the large crater EDS data, and certainly not so large as the apparent discrepancy between EDS and ToF-SIMS data might suggest.

The spot EDX analyses all used a 50 second X-ray collection from a tightly focussed spot at 2nA current and 20kV accelerating voltage, which is a relatively gentle irradiation compared to conditions for wavelength dispersive X-ray analysis (ten times higher beam current and perhaps three times as long for acquisition), where it has been established that alkali migration occurs. X-ray maps which gave very short beam irradiation, less than 0.1 second per micron total, showed high alkali contents in two craters, but also that the alkalis were not distributed evenly at the micron scale. In these craters analyses were taken from scanned areas, with much lower beam irradiation than spot analyses.

TOF-SIMS of Craters

The residues in 5 craters were analyzed by Time-of-Flight Secondary Ion Mass Spectroscopy (ToF-SIMS), using procedures described by Hoppe et al. (Hoppe P., Stadermann F. J., Stephan T., Floss C., Leitner J., Marhas K. K. and Hörz F. (2006) SIMS studies of Allende projectiles fired into Stardust-type aluminum foils at 6 km/sec. *Meteorit. Planet. Sci.* 41, 197–209) and element sensitivities described in Stephan T. (2001) TOF-SIMS in cosmochemistry. *Planet. Space Sci.* 49, 859–906.

Earlier investigations (Hoppe et al. 2006) have shown that TOF-SIMS analysis of the residual matter in hypervelocity impact craters, the projectile material can be identified and its composition can be determined. In the TOF-SIMS instrument, the primary ion beam reaches the sample at an angle of 45°. For samples with high topography, like impact craters, different regions are reached by the ion beam under different orientations, so different areas are analyzed when the sample is rotated. Consequently, the observed differences in the results from impact craters analyzed in two different orientations indicates there is a heterogeneous distribution of the elements in these crater.

One Ni-rich region of crater C2009N,1 was analyzed separately from the rest of the residue in that crater. The TOF-SIMS analysis is most reliable on flat surfaces. The topography of two of the craters complicated the analyses, so each of these was analyzed in two different orientations to assess the effect of topography. In both cases there were large differences in the inferred element/Si ratios.

TOF SIMS DATA TABLE GOES HERE

Table X: Time-of-Flight Secondary Ion Mass Spectrometry Analysis of 5 Craters

est. mass [ng]	C2009N,1 3.4		C2029W,1 17		C2086W,1 178		C2086N,1 3.1		C2091N,1 3.1	
	Si and Cl normalized Ratio	Error	Si and Cl normalized Ratio	Error	Si and Cl normalized Ratio	Error	Si and Cl normalized Ratio	Error	Si and Cl normalized Ratio	Error
Li	2.922	0.388	65.272	9.070	13.110	2.835	2.002	0.817	2.405	0.516
Na	1.487	0.007	174.843	0.340	24.386	0.092	22.227	0.056	8.074	0.020
Mg	0.775	0.002	22.891	0.053	4.031	0.015	0.493	0.004	0.999	0.003
Si	1.000	0.010	1.000	0.070	1.000	0.036	1.000	0.015	1.000	0.011
K	2.746	0.029	159.348	1.032	12.667	0.245	4.699	0.097	1.000	0.016
Ca			27.911	0.168	3.524	0.050	0.734	0.014	2.558	0.874
Sc			22.823	10.891	12.494	4.885	1.100	0.175	0.454	0.031
Ti	0.445	0.048							0.285	0.018
Cr	0.566	0.018							0.138	0.056
Mn	0.495	0.022	0.858	0.183	0.549	0.089	0.091	0.022	0.209	0.034
Fe	0.270	0.010	0.997	0.029	0.270	0.009	0.610	0.060		
Co	0.244	0.050	3.993	1.027	6.487	0.893	0.573	0.007		
Ni	2.296	0.057	3.953	0.349	1.031	0.114	0.167	0.067		